

# Manipulating the helical phase of chiral magnets with electric currents

Jan Masell <sup>1</sup>, Xiuzhen Z. Yu <sup>1</sup>, Naoya Kanazawa <sup>2</sup>, Yoshinori Tokura <sup>1,2,3</sup> and Naoto Nagaosa <sup>1,2</sup>

<sup>1</sup>RIKEN Center for Emergent Matter Science (CEMS), Wako, 351-0198, Japan

<sup>2</sup>Department of Applied Physics, University of Tokyo, Tokyo, 113-8656, Japan

<sup>3</sup>Tokyo College, University of Tokyo, Tokyo 113-8656, Japan

(Dated: June 22, 2022)

The competition between the ferromagnetic exchange interaction and anti-symmetric Dzyaloshinskii-Moriya interaction can stabilize a helical phase or support the formation of skyrmions. While skyrmions and lattices of such are widely studied and known to be manipulable by electric currents, the structurally less complex helical phase is stronger pinned by defects. In thin films of chiral magnets, however, the current density can be large enough to unpin the helical phase and reveal its fascinating dynamics. We theoretically study the dynamics of the helical phase under spin-transfer torques that reveal distinct orientation processes, driven by topological defects in the bulk or induced by edges, and instabilities at larger currents. Our experiments confirm the possibility of on-demand switching the helix orientation by current pulses. Finally, we propose a novel design for memory devices that exploits the orientation of the helical phase as new order parameter.

## INTRODUCTION

In magnetic metals, the magnetization acts on the conduction electrons as a local magnetic field and induces a spin-polarization. When a current is induced, this coupling has consequences for both the electrons and the magnetization beyond the anomalous Hall effect: On the one hand, the spin of the conduction electron locally adapts to the magnetization which can lead to fascinating phenomena such as a topological Hall effect from picking up a real-space Berry phase<sup>1</sup> or an anisotropic magneto-resistance which reflects the anisotropic magnetic order. On the other hand, the magnetization can be spatially inhomogeneous and experiences a spin-transfer torque (STT) due to the local reorientation of the spin-polarized current<sup>2,3</sup>. This electrical control of magnetic states is interesting for both fundamental research and potential applications.<sup>4</sup> For example, it is exploited in commercially available STT-MRAM devices<sup>5</sup> and can be used to move magnetic domain walls<sup>6,7</sup> which might lead to shift register memory devices.<sup>8</sup>

More recently, magnetic skyrmions can be stabilized in chiral magnets<sup>9-11</sup> and arouse great interest because of their nanometer size,<sup>12,13</sup> non-trivial realspace topology,<sup>14,15</sup> and high mobility<sup>16-19</sup> which is interesting for various applications.<sup>20,21</sup> In simple chiral ferromagnets like FeGe, spin-orbit coupling induces an antisymmetric Dzyaloshinskii-Moriya exchange interaction<sup>22,23</sup> which can stabilize skyrmion lattices at certain magnetic fields and temperatures. However, the predominant magnetic phase below the Curie temperature is not a skyrmion lattice but a topologically trivial (multidomain) helical phase.<sup>24-26</sup> Figure 1 shows how the magnetization in the helical phase winds in the plane perpendicular to the  $q$ -vector, which defines the orientation of the phase. When applying a magnetic field,  $q$  and the orientation of the helical phase can be rotated.<sup>27</sup> When applying an electric current, in turn, the helical phase and its orientation usually stay pinned. The reason is that, in contrast to the easily manipulable skyrmion lattice, the helical phase features one extra translation invariant direction perpendicular to its  $q$ -vector. In this direction the helical phase is softer against deformations<sup>28</sup> which leads

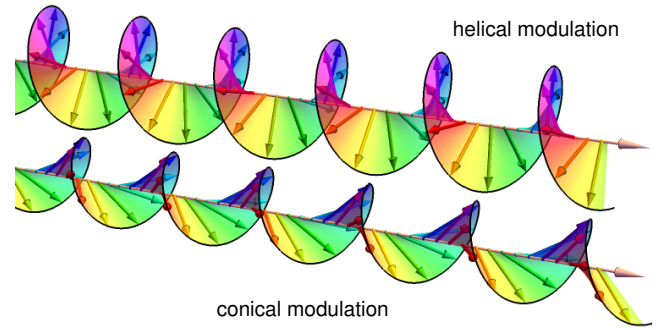


**Fig. 1: Schematic drawing of helical and conical magnetization textures.** In the helical phase, the magnetization rotates in the plane perpendicular to the  $q$ -vector. Spin-transfer torques drive the helical state out of equilibrium into a conical state where the magnetization tilts towards the  $q$ -axis.

to stronger pinning at defects<sup>29,30</sup> such that very high current densities are required for depinning. So far, studies of the dynamics were limited to the time-reversal symmetry breaking effect of the current, which induces a finite cone angle<sup>31,32</sup>

$$\sin \phi \propto \mathbf{j} \cdot \hat{\mathbf{q}}, \quad (1)$$

schematically shown in Figure 1, irrespective of whether the helix is pinned or mobile.

In this paper, we study the current-induced dynamics and collapse of the moving helical phase in chiral magnets. Our large-scale numerical simulations reveal a defect-driven transition from a multidomain to single domain helical phase with  $q \parallel j$  deep in the bulk which can be understood from simple analytical arguments. In turn, at one edge, a new single domain helical phase with  $q \perp j$  enters the system because of the sliding motion. As we show by detailed analytical and numerical calculations, the stability of the helical phase depends on its orientation relative to the current  $q \cdot j$  which results in a various stability related effects, including that the phase with  $q \perp j$  is inherently unstable. Our experiments confirm the current-induced reorientation in a thin specimen of FeGe. We propose that this orientation process could be exploited

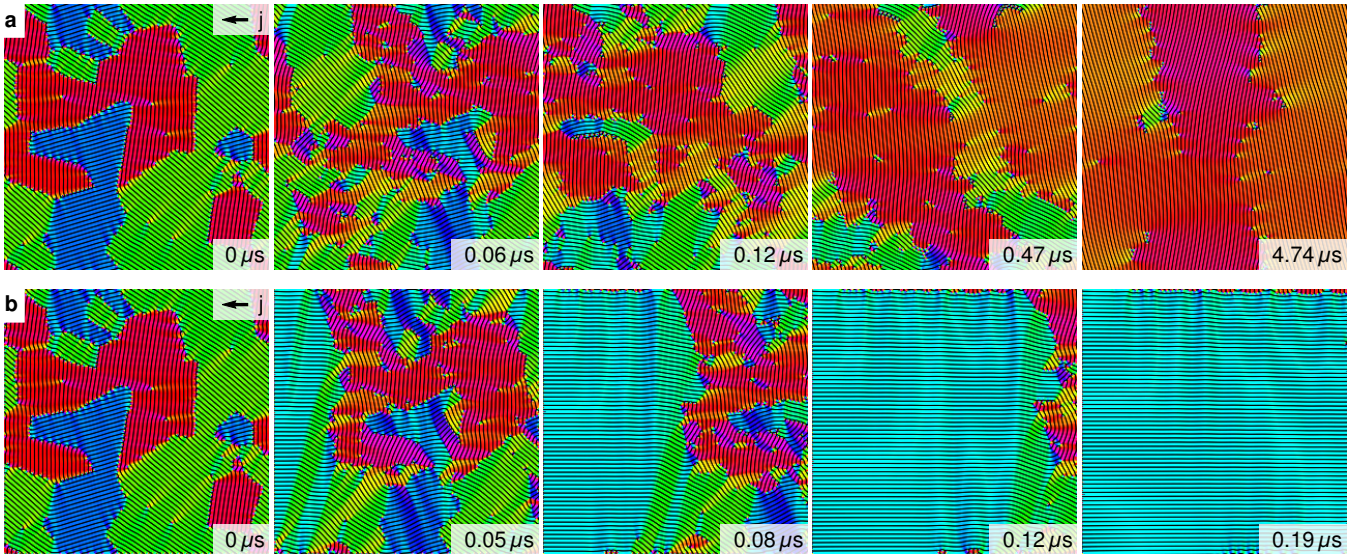


**Fig. 2: Snapshots of the current-induced ordering process of a multidomain helical phase in simulations.** The panels show the magnetization at times  $t$  as indicated. With periodic boundary conditions, **a**, the dynamics are dominated by defects which order the helix with  $\mathbf{q} \parallel \mathbf{j}$ . In turn, in a finite size system with open (Neumann) boundary conditions, **b**, the old pattern is pushed out of the system and replaced by a helical phase with  $\mathbf{q} \perp \mathbf{j}$ . The color encodes the local orientation  $\hat{\mathbf{q}}$  of the helix. Additionally, darker color encodes a larger  $m_z > 0$  and lighter color encodes a larger cone angle. Results are obtained for  $\mathbf{j} = -1.6 \times 10^{11} \text{ A/m}^2 \hat{\mathbf{x}}$  on a system of size  $4.47 \times 4.47 \mu\text{m}^2$ .

in novel storage devices, e.g., MRAM cells<sup>5</sup> or memristors<sup>33</sup> which measure an orientation dependent resistance.

## RESULTS

The orientation of the helical phase is usually pinned by anisotropies which leads to a multidomain state when cooling below the Curie temperature.<sup>25,27</sup> Here, in our theoretical analysis, we neglect such orientational anisotropies as we expect their effects to be weak compared to the strong current. We also neglect the effect of the spin-orbit coupling induced torque in chiral magnets.<sup>34</sup> However, the multidomain character turns out to be crucial for the current-induced dynamics.

The evolution of the magnetization during our simulation is shown in Figure 2a and Supplementary Movie S1 where we apply a current density of  $j = 1.6 \times 10^{11} \text{ A/m}^2$  using periodic boundary conditions. On large timescales, the initially multidomain helical phase transforms into a monodomain phase with  $\mathbf{q} \parallel \mathbf{j}$ . This ordering process is driven by the dynamics of defects in the helical texture which carry a non-quantized topological charge

$$Q = \iint_{\Omega} \hat{\mathbf{m}} \cdot \left( \frac{d\hat{\mathbf{m}}}{dx} \times \frac{d\hat{\mathbf{m}}}{dy} \right) d\mathbf{r} \in \mathbb{R} \quad (2)$$

and naturally arise at the interfaces between differently oriented helical domains.<sup>35</sup> Here,  $\hat{\mathbf{m}}$  is the normalized magnetization and  $\Omega$  is an adequately chosen finite area around the defects which can comprise disclinations<sup>35</sup>, dislocations<sup>36</sup>, and skyrmions.<sup>37</sup> The topological charge distribution for Figure 2a (at  $t = 0.47 \mu\text{s}$ ) is shown in Figure 3, including a magnified view on a positively and a negatively charged dislocation.

At this relatively small current density, the motion of defects is confined to lanes defined by the helical background. This background moves uniformly at a velocity  $\mathbf{v} \propto -\mathbf{j}$  parallel to the current whereas defects with a charge  $Q \neq 0$  experience a transverse velocity component similar to the skyrmion Hall effect.<sup>38,39</sup> This extra transverse velocity is indicated in Figure 3 and can be observed in Supplementary Movie S2. Due to their transverse motion, the defects comb their confining lanes such that  $\mathbf{q} \parallel \mathbf{j}$ . Moreover, oppositely charged

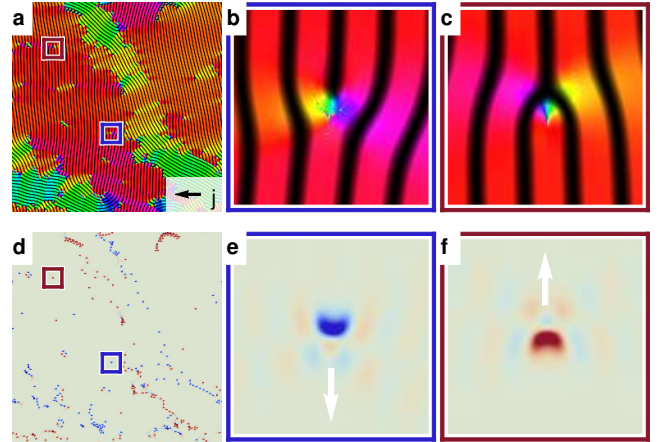


**Fig. 3: Motion of defects in the current-driven helical phase.** The driven helical phase, **a**, is combed by defects such as the dislocations in **b** (blue frame) and **c** (red frame), using the color code of Figure 2. Panels **d-f** show the corresponding topological charge density, Equation (2), with  $Q > 0$  (blue) to  $Q = 0$  (pale green) to  $Q < 0$  (red). The write arrow in **e** and **f** indicates the downwards/upwards motion of the oppositely charged defects.

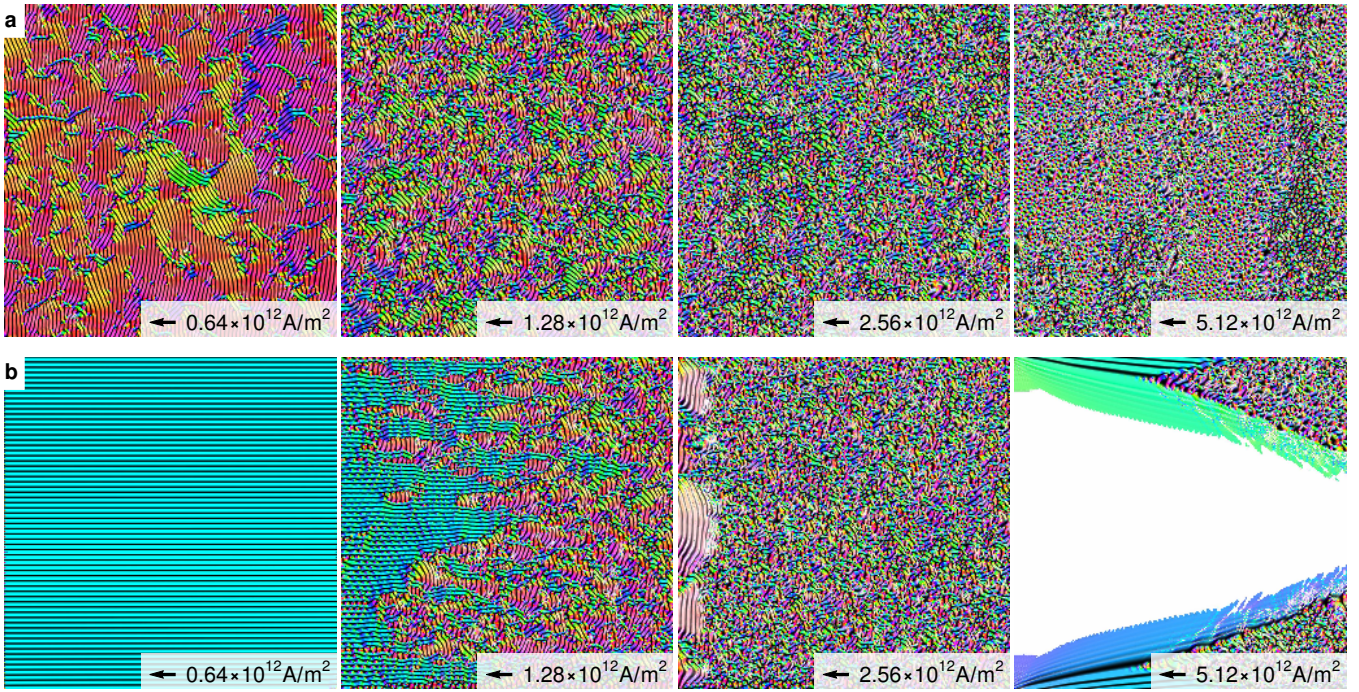


**Fig. 4: Magnetization textures above the instability of the driven helical phase.** The panels show snapshots after simulating a sufficiently long timespan with periodic boundary conditions, **a**, or open (Neumann) boundary conditions, **b**, until the steady state is established. The setup and color code are the same as in Figure 2 but every panel is obtained for a different current density  $\mathbf{j} = -j\hat{x}$  with  $j$  as indicated. In the last panel of **b**, the magnetization in the white area is almost polarized in the direction of the current such that the definition of a local  $\mathbf{q}$ -vector does not make sense.

defects can annihilate and equally charged defects can form skyrmions that eventually decay under pressure,<sup>40</sup> which decreases the number of defects. Further details are provided in the Supplementary Material.

At the edges of a finite size system we observe different dynamics: As shown in Figure 2b and Supplementary Movie S3, the collective sliding motion pushes the initial magnetic texture over one edge out of the system. On the opposite edge, the empty space is filled by a newly entering phase with  $\mathbf{q} \perp \mathbf{j}$  until the entire system is again in a monodomain state. Exceptions are observed at the transverse edges where defects might enter because of their charge-induced dynamics. We confirmed the order  $\mathbf{q} \perp \mathbf{j}$  due to edges also for other orientations of the current.

For larger current densities, the helical phase becomes unstable. One critical current is set by the analogue of the *Walker breakdown*<sup>41</sup> of magnetic domain walls. Above a critical current, the helicity of a domain wall gets unpinned, resulting in a steady rotation of the magnetization inside the domain wall on top of the translational motion. In an idealized helical phase, this Walker-esque breakdown occurs everywhere simultaneously because of the screw-rotational symmetry, which is equivalent to closing the current-induced cone in Equation (1) such that  $\mathbf{m} \parallel \mathbf{j}$ . For FeGe we obtain the orientation dependent critical current  $\mathbf{j}_c \cdot \hat{\mathbf{q}} \approx 2.5 \times 10^{12} \text{ A/m}^2$  if the wavelength is the equilibrium wavelength  $\lambda \approx 70 \text{ nm}$ . An expanded wavelength above the equilibrium value increases the critical current up to a factor two whereas decreasing the

wavelength reduces the critical current. Moreover, our detailed calculations in the Supplementary Material reveal that in the helix with  $\mathbf{q} \perp \mathbf{j}$  some modes soften already below the Walker breakdown which triggers the reduction of the wavenumber. An ideal helix would therefore undergo a series of instabilities to larger wavelengths until it finally saturates at the Walker breakdown. However, in a more realistic setup with defects, the instabilities can be locally activated. As a result, defects occasionally detach from their helical ties, leaving the system with only a short-range order, see Figure 4a, first panel, and Supplementary Movie S4. At higher currents, more defects proliferate and the helical background becomes more transparent which leads to a gradually shorter ranged order, see Figure 4a, which establishes instead of the inplane polarized state.

Another instability of the driven helical phase owes even more directly to its low-dimensional texture, namely the translational invariance and thus softer excitation spectrum perpendicular to  $\mathbf{q}$ .<sup>28</sup> In fact, we find that *any* finite current perpendicular to  $\mathbf{q}$  triggers an instability which spontaneously breaks the continuous translational symmetry with

$$k_{\perp} \propto \mathbf{j} \cdot (\hat{\mathbf{z}} \times \hat{\mathbf{q}}). \quad (3)$$

Our analytical results, presented in the Supplementary Material, show that the amplitude of this instability grows as  $\propto \exp[(j/j_c)^4(t/t_0)]$  which is very slow for small currents. Moreover, we ran simulations to determine the new steady state, which for smaller current densities is slightly wavy,

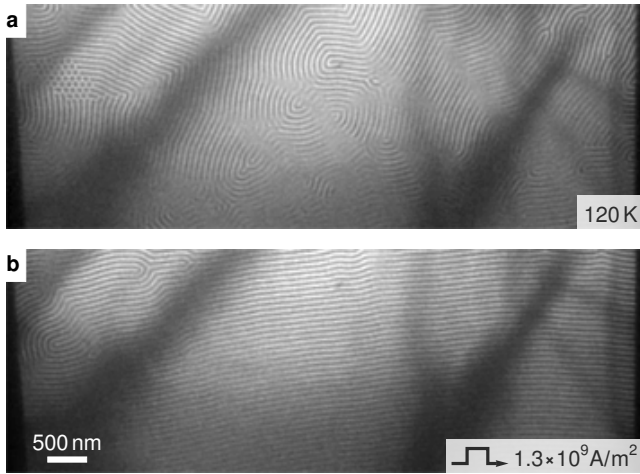


**Fig. 5: Experimental observation of current-induced order in the helical phase.** The panels show Lorentz TEM images of a 150 nm thick film of FeGe at 120 K before and after a current pulse. The initial magnetization, **a**, shows a multidomain helical phase (stripes) and a small skyrmion cluster (dots on left side). After a current pulse with  $j = 1.3 \times 10^9 \text{ A/m}^2$  for 0.5 ms in the horizontal direction, **b**, the magnetization is in an almost defect-free helical state, ordered with  $\mathbf{q} \perp \mathbf{j}$ .

for larger currents turns zig-zag, and at highest currents becomes unstable towards the proliferation of dislocations and skyrmions<sup>42,43</sup>. In Figure 4b and the corresponding Supplementary Movies S5-S8 we show the steady state magnetization obtained from simulations with successively larger currents for the system known from Figure 2b. In the first panel, the inherent instability is not observed as its timescale is smaller than the time needed to pass once through the system, similar to Figure 2b. In the second panel, the inherent instability occurs faster and thus can be observed close to the edge where it destroys the helical order. In the third panel, where the current is above the Walker breakdown, the length scale of the inherent instability is too small to be observed. Instead, patches of the also unstable but more slowly decaying phase with  $\mathbf{q} \parallel \mathbf{j}$  eventually burst from the edge and decay into the fluctuating background via the Walker breakdown. For a current above twice the Walker breakdown, fourth panel, we finally observe a large scale inplane polarized phase, here shown in white, which seeds at the edge but is unstable against both the seemingly laminar and turbulent phases that enter from the transverse edges.

We also experimentally confirm the possibility of current-induced order in the helical phase, using the experimental setup from Ref. 44 where current pulses can be applied through a  $20 \times 20 \times 0.15 \mu\text{m}^3$  film of FeGe. Figure 5a shows a Lorentz TEM image of the initial state after cooling to 120 K. The magnetization appears to be in a multidomain helical phase and also a skyrmion cluster can be spotted. After applying a single current pulse of  $1.3 \times 10^9 \text{ A/m}^2$  for 0.5 ms, the helical phase is ordered with  $\mathbf{q} \perp \mathbf{j}$  and includes only very few dislocation defects, see Figure 5b. This observation is in agreement with our theoretical prediction on the edge-induced

order for the unpinned helical phase at small currents. However, we do not observe the defect-induced order  $\mathbf{q} \parallel \mathbf{j}$  predicted in our simulations, probably because the sample size is much too small.

The current-induced helical orientation can be used to all-electrically imprint an anisotropic pattern onto the magnetization. Such a pattern shows an anisotropic magnetoresistance dependent on the helical orientation  $\mathbf{q}$ . We suggest that this effect might be exploited for novel spintronics devices which make use of the helical orientation as an order parameter. As an example, the working principle of a helix-based MRAM cell is illustrated in Figure 6a. The orientation of the helical phase in a small square-shaped sample encodes binary information (states “0” and “1”). Information can be written by a current pulse in the horizontal (“0”  $\rightarrow$  “1”) or vertical direction (“1”  $\rightarrow$  “0”), while reading only requires a small test current in the horizontal direction to probe the anisotropic resistance. Our simulations of the switching process are summarized in Figure 6b, where we started from state “0” and applied a rectangular current pulse in the horizontal direction. The current pulse is chosen long enough to establish a driven steady state, shown in the Supplementary Material. The panels show the final magnetization as function of the applied current and the Gilbert damping.<sup>45</sup> For very high current densities above

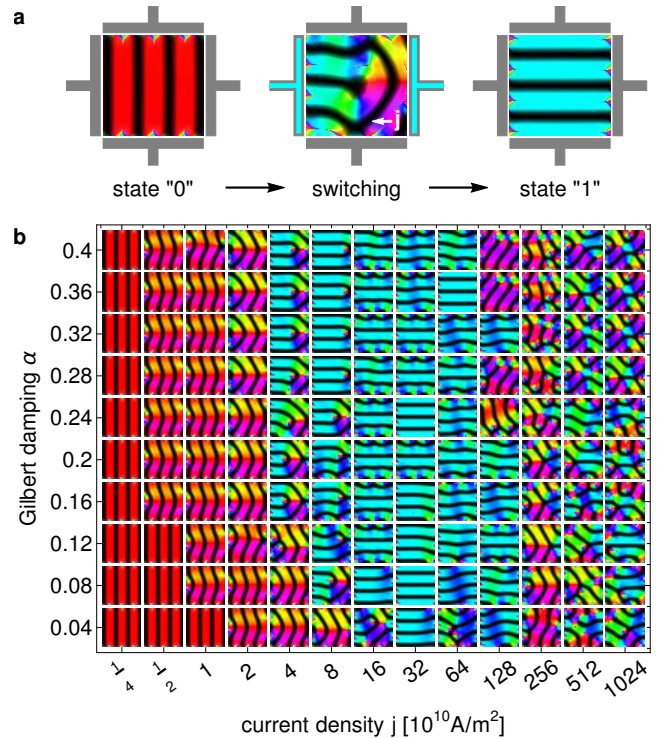


**Fig. 6: A magnetic memory based on the helical orientation.** **a**, Information is encoded in the orientation of the helical phase, here inside a  $227 \times 227 \text{ nm}^2$  square-shaped element, and can be written by current pulses in the horizontal direction, writing a “1”, and the vertical direction, writing a “0”. **b**, relaxed magnetization after a long current pulse, as function of the current density  $j$  and Gilbert damping  $\alpha$ .

$j = 1.28 \times 10^{12}$  A/m<sup>2</sup>, the instabilities in Figure 5b, third panel and fourth panel, induce strong fluctuations and render the final state rather random. For low current densities, in turn, no switching is observed. In principle, the (current-free) helix with orientation  $\mathbf{q}$  fulfills the boundary condition at the edge characterized by the normal vector  $\hat{\nu} \parallel \mathbf{q}$  for all phase shifts and therefore is not subject to any pinning forces. At the perpendicular edges, however, this is not the case and the helix gets an extra surface twist. In combination, at low currents, the helix is pinned because of the extra surface twists in the corners of the square-shaped element. Consequently, upon increasing the current, first the central part of the helix is pushed over the edge while the twisted texture in the corners is still pinned. Moreover, the onset of the newly entering helical phase appears as a dislocation which strongly bends the helical stripes and therefore also has a repulsive interaction with the edge. For an increasing current density, we thus observe a series of incomplete switching processes, owed to the complex hierarchy of critical currents. According to our simulations, the Gilbert damping only has a minor influence on the steady state magnetization which is to a large proportion successfully switched in a range of  $j = 8-128 \times 10^9$  A/m<sup>2</sup>. Only for the smallest shown values, where the destabilizing dynamics of defects are most pronounced, the window for successful switching is narrowed. Note that these results, as all results shown in the main text, were obtained for a ratio of  $\beta/\alpha = 2$ , where  $\beta$  is the non-adiabatic parameter of the spin-transfer torque.<sup>46</sup> In the Supplementary Material, we show the corresponding data for  $\beta/\alpha = 1$ , which does not have a significant difference in the switching success despite the factor 2 smaller drift velocity of the magnetic texture. We also show data for a larger MRAM cell, which features smaller critical currents for switching.

More unconventional ideas can also exploit that the information encoded in the helical orientation is not binary. In principle, a current can be applied in any direction to realize any orientation of the helix in a device with more than only two logic states but here we restricted the analysis to two states because of the geometric anisotropy of the square-shaped cell. Moreover, in a larger cell the critical currents drop and hence we can use the read-out currents to simultaneously induce fractions of new helical order at the edge while probing the system. As a result, every read-out operation lowers the resistance of the element which is a key element for memristive computing.<sup>33</sup>

## CONCLUSIONS

In this work, we have analyzed the spin-transfer torque induced dynamics of the helical phase of chiral magnets, how it orders at small currents and how it turns disordered above a critical current. For large systems, we theoretically predict a reorientation transition from an initially multidomain helical phase to a monodomain phase with  $\mathbf{q} \parallel \mathbf{j}$ , driven by the dynamics of topological defect. At the edge of the system, however, we expect a new helical phase with  $\mathbf{q} \perp \mathbf{j}$  to enter. Our experimental observation in a thin plate of FeGe confirms this

edge-induced ordering mechanism. Above the critical current, where defects are no longer bound to helical lanes, the ordering mechanism in the bulk breaks down but edge-induced order can still be obtained. However, this edge-induced order is intrinsically unstable and might decay to a waved helix at low currents or show a cascade of possible instabilities at large currents as shown in Figure. 4b.

In conclusion, the helical phase of chiral magnets seemed featureless compared to magnetic skyrmions which appear in the same class of materials. We disprove this prejudice, revealing the fascinating and non-trivial dynamics which will be analyzed further in the future and unleash the helical orientation as a new complex order parameter for future applications.

## METHODS

### Theoretical model

We describe the magnetization at zero temperature by a two-dimensional non-linear sigma model which includes only the leading order terms,

$$E[\hat{\mathbf{m}}] = \int d^2r \left[ \frac{J}{2} (\nabla \hat{\mathbf{m}})^2 + D \hat{\mathbf{m}} \cdot (\nabla \times \hat{\mathbf{m}}) \right], \quad (4)$$

where  $\hat{\mathbf{m}} = \mathbf{M}/M_s$  is the normalized magnetization. We use  $J = 17.5$  pJ/m for the ferromagnetic exchange,  $D = 1.58$  mJ/m<sup>2</sup> for the DMI,  $M_s = 384$  kA/m for the saturation magnetization,<sup>47</sup> and neglect the influence of demagnetization fields. The dynamics of the magnetization are governed by the Landau-Lifshitz-Gilbert-Slonczewski equation<sup>46</sup>

$$\begin{aligned} \frac{d}{dt} \hat{\mathbf{m}} = & -\gamma \hat{\mathbf{m}} \times \mathbf{B}_{\text{eff}} + \alpha \hat{\mathbf{m}} \times \frac{d}{dt} \hat{\mathbf{m}} \\ & + \frac{P\mu_B}{eM_s(1+\beta^2)} \left( (\mathbf{j} \cdot \nabla) \hat{\mathbf{m}} - \beta \hat{\mathbf{m}} \times (\mathbf{j} \cdot \nabla) \hat{\mathbf{m}} \right), \end{aligned} \quad (5)$$

where  $\gamma$  is the gyromagnetic ratio,  $\mathbf{B}_{\text{eff}}$  is the effective magnetic field,  $\alpha$  is the Gilbert damping,  $P$  is the spin polarization,  $e > 0$  is the electron charge,  $\beta$  is the non-adiabatic damping parameter, and  $\mathbf{j}$  is the current density. For all results shown in the main text, we used  $\beta = 2\alpha$  and  $P = 1$ . Figures 2 and 4 are computed for  $\alpha = 0.1$  and the current is smoothly increased over a timespan of approximately 47 ns. For Figure ??, this timespan is reduced to 0.12 ns.

### Simulations

Simulations of the current-driven magnetization have been performed using a self-written GPU-accelerated software which uses single precision. Spatial derivatives are discretized by  $\mathcal{O}(a^4)$  finite difference schemes, including the solution of the LLGS equation on the open (Neumann) edges, to minimize unphysical numerical lattice anisotropies.<sup>48</sup> Time-integration is performed using a standard fourth order Runge-Kutta algorithm which includes a normalization of the magnetization after each iteration step. We use a discretization of

$a = \lambda/32$ , where  $\lambda \approx 70$  nm is the helical wavelength in equilibrium, with additional checks for  $a = \lambda/16$ . An exception is the last panel of Figure 2a which was only computed for  $a = \lambda/16$  (this does not qualitatively influence the result but makes very long timescales more easily accessible). The systems shown in Figures 2 and 4 contain  $2048 \times 2048$  lattice sites and in Figure ??  $104 \times 104$  lattice sites. Additional checks have been performed using a self-written CPU code with  $\mathcal{O}(a^8)$  finite difference schemes and double precision.<sup>49</sup> The initial multidomain helix in Figures 2 and 4 was obtained by initializing a random tessellation which is then relaxed using standard methods. The initial state in Figure ?? was artificially initialized as a single domain state and then

relaxed.

### Lorentz TEM observations

We settle a FeGe thin plate with dimensions  $20 \times 20 \times 0.15 \mu\text{m}^3$  on a TEM holder with electric contacts (Gatan HC3500). The thin plate of FeGe was cooled to 120 K in a transmission electron microscope (JEM2800, JEOL) and simultaneously imaged at a Lorentz TEM mode. We apply one current pulse of 0.5 ms width and with  $1.3 \times 10^9 \text{ A/m}^2$  amplitude through the thin plate. The experimental setup is the same as used in Ref. 44 and the sample has a notch on one side but the data shown here is taken on the other side of the sample, far away from the notch.

- <sup>1</sup> Binz, B. & Vishwanath, A. Chirality induced anomalous-Hall effect in helical spin crystals. *Physica B Condens. Mater* **403**, 1336–1340 (2008).
- <sup>2</sup> Slonczewski, J.C. Current-driven excitation of magnetic multilayers. *J. Magn. Magn. Mater.* **159**, L1–L7 (1996).
- <sup>3</sup> Berger, L. Emission of spin waves by a magnetic multilayer traversed by a current. *Phys. Rev. B* **54**, 9353 (1996).
- <sup>4</sup> Chappert, C., Fert, A. & Van Dau, F. The emergence of spin electronics in data storage. *Nat. Mater.* **6**, 813–823 (2007).
- <sup>5</sup> Bhatti, S. et al. Spintronics based random access memory: a review. *Mater. Today* **20**, 530–548 (2017).
- <sup>6</sup> Berger, L. Exchange interaction between ferromagnetic domain wall and electric current in very thin metallic films. *J. Appl. Phys.* **55**, 1954 (1984).
- <sup>7</sup> Freitas, P. P. & Berger, L. Observation of sd exchange force between domain walls and electric current in very thin Permalloy films. *J. Appl. Phys.* **57**, 1266 (1985).
- <sup>8</sup> Parkin, S. S. P., Hayashi, M. & Thomas, L. Magnetic Domain-Wall Racetrack Memory. *Science* **320**, 190–194 (2008).
- <sup>9</sup> Bogdanov, A. N. & Yablonskii, D. A. Thermodynamically stable "vortices" in magnetically ordered crystals. The mixed state of magnets. *J. Exp. Theor. Phys.* **68**, 101 (1989).
- <sup>10</sup> Mühlbauer, S. et al. Skyrmion Lattice in a Chiral Magnet. *Science* **323**, 915–919 (2009).
- <sup>11</sup> Yu, X. Z. et al. Real-space observation of a two-dimensional skyrmion crystal. *Nature* **465**, 901–905 (2010).
- <sup>12</sup> Fert, A., Reyren, N. & Cros, V. Magnetic skyrmions: advances in physics and potential applications. *Nat. Rev. Mater.* **2**, 17031 (2017).
- <sup>13</sup> Everschor-Sitte, K., Masell, J., Reeve, R. M. & Kläui, M. Perspective: Magnetic skyrmions – Overview of recent progress in an active research field. *J. Appl. Phys.* **124**, 240901 (2018).
- <sup>14</sup> Milde, P. et al. Unwinding of a Skyrmion Lattice by Magnetic Monopoles. *Science* **340**, 1076–1080 (2013).
- <sup>15</sup> Nagaosa, N. & Tokura, Y. Topological properties and dynamics of magnetic skyrmions. *Nat. Nanotechnol.* **8**, 899–911 (2013).
- <sup>16</sup> Jonietz, F. et al. Spin Transfer Torques in MnSi at Ultralow Current Densities. *Science* **330**, 1648–1651 (2010).
- <sup>17</sup> Schulz, T. et al. Emergent electrodynamics of skyrmions in a chiral magnet. *Nat. Phys.* **8**, 301–304 (2012).
- <sup>18</sup> Yu, X. Z. et al. Skyrmion flow near room temperature in an ultralow current density. *Nat. Commun.* **3**, 988 (2012).
- <sup>19</sup> Woo, S. et al. Observation of room-temperature magnetic skyrmions and their current-driven dynamics in ultrathin metallic ferromagnets. *Nat. Mater.* **15**, 501–506 (2016).
- <sup>20</sup> Fert, A., Cros, V. & Sampaio, J. Skyrmions on the track. *Nat. Nanotechnol.* **8**, 152–156 (2013).
- <sup>21</sup> Masell, J. & Everschor-Sitte, K. Current-Induced Dynamics of Chiral Magnetic Structures: Creation, Motion, and Applications. Preprint at <https://arxiv.org/abs/2004.13535> (2020).
- <sup>22</sup> Dzyaloshinsky, I. A thermodynamic theory of "weak" ferromagnetism of antiferromagnetics. *J. Phys. Chem. Solids* **4**, 241–255 (1958).
- <sup>23</sup> Moriya, T. Anisotropic Superexchange Interaction and Weak Ferromagnetism. *Phys. Rev.* **120**, 91 (1960).
- <sup>24</sup> Dzyaloshinskii, I. E. The Theory of Helicoidal Structures in Antiferromagnets. II. Metals. *J. Exp. Theor. Phys.* **20**, 223 (1965).
- <sup>25</sup> Bak, P. & Jensen, M. H. Theory of helical magnetic structures and phase transitions in MnSi and FeGe. *J. Phys. C: Solid State Phys.* **13**, L881 (1980).
- <sup>26</sup> Uchida, M., Onose, Y., Matsui, Y. & Tokura, Y. Real-Space Observation of Helical Spin Order. *Science* **20**, 359–361 (2006).
- <sup>27</sup> Bauer, A. et al. Symmetry breaking, slow relaxation dynamics, and topological defects at the field-induced helix reorientation in MnSi. *Phys. Rev. B* **95**, 024429 (2017).
- <sup>28</sup> Belitz, D., Kirkpatrick, T. R. & Rosch, A. Theory of helimagnons in itinerant quantum systems. *Phys. Rev. B* **73**, 054431 (2006).
- <sup>29</sup> Iwasaki, J., Mochizuki, M. & Nagaosa, N. Universal current-velocity relation of skyrmion motion in chiral magnets. *Nat. Commun.* **4**, 1463 (2013).
- <sup>30</sup> Hoshino, S. & Nagaosa, N. Theory of the magnetic skyrmion glass. *Phys. Rev. B.* **97**, 024413 (2018).
- <sup>31</sup> Goto, K., Katsura, H. & Nagaosa, N. Current-induced dynamics of spiral magnet. Preprint at <https://arxiv.org/abs/0807.2901> (2008).
- <sup>32</sup> Nagaosa, N. Emergent inductor by spiral magnets. *Jpn. J. Appl. Phys.* **58**, 120909 (2019).
- <sup>33</sup> Yang, J., Strukov, D. & Stewart, D. Memristive devices for computing. *Nat. Nanotechnol.* **8**, 13–24 (2013).
- <sup>34</sup> Hals, K. M. D. & Brataas, A. Spin-transfer torques in helimagnets. *Phys. Rev. B* **87**, 174409 (2013).
- <sup>35</sup> Schoenherr, P. et al. Topological domain walls in helimagnets. *Nat. Phys.* **14**, 465–468 (2018).
- <sup>36</sup> Dussaux, A. et al. Local dynamics of topological magnetic defects in the itinerant helimagnet FeGe. *Nat. Commun.* **7**, 12430 (2016).

- <sup>37</sup> Müller, J. et al. Magnetic Skyrmions and Skyrmion Clusters in the Helical Phase of  $\text{Cu}_2\text{OSeO}_3$ . *Phys. Rev. Lett.* **119**, 137201 (2017).
- <sup>38</sup> Jiang, W. et al. Direct observation of the skyrmion Hall effect. *Nat. Phys.* **13**, 162–169 (2017).
- <sup>39</sup> Litzius, K. et al. Skyrmion Hall effect revealed by direct time-resolved X-ray microscopy. *Nat. Phys.* **13**, 170–175 (2017).
- <sup>40</sup> Heil, B., Rosch, A. & Masell, J. Universality of annihilation barriers of large magnetic skyrmions in chiral and frustrated magnets. *Phys. Rev. B* **100**, 134424 (2019).
- <sup>41</sup> Schryer, N. L. & Walker, L. R. The motion of  $180^\circ$  domain walls in uniform dc magnetic fields. *J. Appl. Phys.* **45**, 5406 (1974).
- <sup>42</sup> Lin, S.-Z., Reichhardt, C., Batista, C. D. & Saxena, A. Driven Skyrmions and Dynamical Transitions in Chiral Magnets. *Phys. Rev. Lett.* **110**, 207202 (2013).
- <sup>43</sup> Lin, S.-Z. Edge instability in a chiral stripe domain under an electric current and skyrmion generation. *Phys. Rev. B* **94**, 020402(R) (2016).
- <sup>44</sup> Yu, X. Z. et al.. Motion tracking of 80-nm-size skyrmions upon directional current injections. *Sci. Adv.* **6**, eaaz9744 (2020).
- <sup>45</sup> Gilbert, T. A phenomenological theory of damping in ferromagnetic materials. *IEEE Trans. Magn.* **40**, 3443–3449 (2004).
- <sup>46</sup> Zhang, S. & Li, Z. Roles of Nonequilibrium Conduction Electrons on the Magnetization Dynamics of Ferromagnets. *Phys. Rev. Lett.* **93**, 127204 (2004).
- <sup>47</sup> Beg, M. et al. Ground state search, hysteretic behaviour and reversal mechanism of skyrmionic textures in confined helimagnetic nanostructures. *Sci. Rep.* **5**, 17137 (2015).
- <sup>48</sup> Miltat, J. E. & Donahue, M. J. *Numerical Micromagnetics: Finite Difference Methods in Handbook of Magnetism and Advanced Magnetic Materials* (eds Kronmüller, H., Parkin, S., Miltat, J. E. & Scheinfein, M. R.) (Wiley, 2007).
- <sup>49</sup> Müller, J. *Magnetic Skyrmions and Topological Domain Walls* (Universität zu Köln, Cologne, 2018).

## Additional information

Supplementary information is available in the online version of the paper. Correspondence and reasonable requests for materials should be addressed to J.M. (simulations) and X.Y. (experimental data).

## Acknowledgments

J.M. thanks V. Kravchuk and M. Garst for the helpful discussions. This work was financially supported by Grants-In-Aid for Scientific Research (A) (grant no. 18H03676 and 19H00660) from the Japanese Society for the Promotion of Science (JSPS) and the Japan Science and Technology Agency (JST) CREST program (grant number JPMJCR1874), J.M. acknowledges financial support by JSPS (project No. 19F19815) and the Alexander von Humboldt foundation.

## Author contributions

J.M. and N.N. conceived the project and wrote the manuscript. J.M. performed the calculations, simulations, and developed the code. J.M. and N.N. analyzed the data. X.Z.Y. designed and fabricated the FeGe microdevice and performed the Lorentz TEM measurements. N.K. and Y.T. synthesized the bulk FeGe crystal.

## Competing interests

The authors declare no competing interests.

## Supplementary Material for "Manipulating the helical phase of chiral magnets with electric currents"

Jan Masell,<sup>1</sup> Xiuzhen Z. Yu,<sup>1</sup> Naoya Kanazawa,<sup>2</sup> Yoshinori Tokura,<sup>1,2,3</sup> and Naoto Nagaosa<sup>1,2</sup>

<sup>1</sup>*RIKEN Center for Emergent Matter Science (CEMS), Wako, 351-0198, Japan*

<sup>2</sup>*Department of Applied Physics, University of Tokyo, Tokyo, 113-8656, Japan*

<sup>3</sup>*Tokyo College, University of Tokyo, Tokyo 113-8656, Japan*

We here present details on the analytical and numerical solutions of the theoretical model.

### DETAILS ON THEORETICAL RESULTS

In contrast to the main text, where we focused on FeGe and expressed all results in the units of this material, we express the results in this Supplementary Material in the generalized parameters of the theory without assuming a specific material. The parameters for FeGe are taken from Ref. S1 and given in the Methods section of the main text.

#### The model

We consider a two-dimensional chiral magnet which stabilizes a helical phase with a wavelength  $\lambda = 2\pi/q$  much larger than the distance  $a$  between atomic cells. In this limit,  $\lambda \gg a$ , a continuum model is a good approximation. Moreover, we assume that magnetostatic interactions are irrelevant and that the temperature is low enough such that the magnetization amplitude is given by the saturation value,  $\mathbf{m} = \mathbf{M}/M_s$ . The energy functional thus reads simply

$$E[\mathbf{m}] = \int d^2r \frac{J}{2} (\nabla \mathbf{m})^2 + D \mathbf{m} \cdot (\nabla \times \mathbf{m}) \quad (\text{S1})$$

where  $J$  is the magnetic stiffness (in some publications  $J = 2A$  is used) and  $D$  is the Dzyaloshinskii-Moriya interaction<sup>S2</sup> (DMI) which stabilizes right-handed screw rotations for  $D > 0$ . Because of a spin rotation symmetry, our results immediately also apply to thin films with interfacial DMI<sup>S3,S4</sup> where Néel-type spirals are stabilized instead. In an infinitely large system without edges or impurities, the magnetic texture  $\mathbf{m}_0$  which minimizes Eq. (S1) is a right-handed helix

$$\mathbf{m}_0(\mathbf{r}) = (\hat{\mathbf{z}} \times \hat{\mathbf{q}}) \cos(\mathbf{q} \cdot \mathbf{r}) + \hat{\mathbf{z}} \sin(\mathbf{q} \cdot \mathbf{r}), \quad \text{with} \quad \mathbf{q} = \frac{D}{J} \hat{\mathbf{q}}. \quad (\text{S2})$$

In our convention, the  $\hat{\mathbf{z}}$ -direction is perpendicular to the two-dimensional plane. Without further anisotropies, the system is translation and rotation invariant such that the direction of  $\hat{\mathbf{q}}$  and the origin of the coordinate system can be chosen arbitrarily.

For variations of the magnetization on the order of a lattice constant, the effective spin-transfer torque is analyzed in Refs. S5, S6. Here, we assume that these extra effects are negligible as the magnetization varies on large length scales. The dynamics of the magnetization far below the Curie temperature are given by the Landau-Lifshitz-Gilbert-Slonczewski equation<sup>S7,S8,S9,S10</sup>

$$d_t \mathbf{m} = -\gamma \mathbf{m} \times \mathbf{B}_{\text{eff}} - (\mathbf{v}_e \cdot \nabla) \mathbf{m} + \alpha \mathbf{m} \times d_t \mathbf{m} + \beta \mathbf{m} \times (\mathbf{v}_e \cdot \nabla) \mathbf{m} \quad (\text{S3})$$

where  $\gamma$  is the gyromagnetic ratio,  $\mathbf{B}_{\text{eff}} = -\delta E[\mathbf{m}]/(M_s \delta \mathbf{m})$  is the effective magnetic field,  $\alpha$  is the Gilbert damping, and  $\beta$  is the non-adiabatic damping parameter.<sup>S10,S11,S12</sup> The current density is written in terms of the drift velocity  $\mathbf{v}_e = -[P\mu_B/eM_s(1 + \beta^2)]\mathbf{j}_e$  with  $\mathbf{j}_e$  the electric current density,  $P$  the polarization,  $\mu_B$  the Bohr magneton, and  $e > 0$  the electron charge.

We will in the following first consider the effectively one-dimensional solution and its stability and then discuss additional properties that arise in more than one dimension.

#### Stationary solution for the defect-free helix and its Walker breakdown

Consider the ideal helix, Eq. (S2), without pinning or defects in an infinitely large system. Let us assume that after applying a constant current density for a sufficiently long time, the system eventually reaches a stationary state, i.e., the magnetization moves with a global velocity  $\mathbf{v}$  but is otherwise constant,  $\mathbf{m}(\mathbf{r}, t) = \mathbf{m}(\mathbf{r} - \mathbf{v}t, 0)$ . We can then derive that this velocity is given

as  $\mathbf{v} = (\beta/\alpha)\mathbf{v}_e$  (see the discussion of Thiele dynamics further below). To more easily find these stationary solutions, it makes sense to cast the LLGS equation, Eq. (S3), into a frame of reference which moves at this velocity  $\mathbf{v}$ :

$$d_t \tilde{\mathbf{m}} = -\gamma \tilde{\mathbf{m}} \times \mathbf{B}_{\text{eff}}^v + \alpha \tilde{\mathbf{m}} \times d_t \tilde{\mathbf{m}} \quad \text{with} \quad \mathbf{B}_{\text{eff}}^v = \mathbf{B}_{\text{eff}} - \frac{\alpha - \beta}{\alpha\gamma} \tilde{\mathbf{m}} \times (\mathbf{v}_e \cdot \nabla) \tilde{\mathbf{m}}. \quad (\text{S4})$$

Here, we have introduced the magnetization in the moving frame  $\tilde{\mathbf{m}}(\mathbf{r}, t) = \mathbf{m}(\mathbf{r} - \mathbf{v}t, t)$  and the effective magnetic field  $\mathbf{B}_{\text{eff}}^v$  which comprises the additional current-induced field.<sup>S13</sup> For the helical phase of Eq. (S2), the effective field becomes  $\mathbf{B}_{\text{eff}}^v = \mathbf{B}_{\text{eff}} - \frac{\alpha - \beta}{\alpha\gamma} \mathbf{v}_e \cdot \mathbf{q}$ , adding a current-induced field in the direction of helical orientation  $\hat{\mathbf{q}}$ . For a finite current density  $v_e > 0$ , a suitable ansatz is therefore the moving conical state  $\tilde{\mathbf{m}}_c$  which still preserves the screw-rotational symmetry in the  $\hat{\mathbf{q}}$ -direction and reads

$$\tilde{\mathbf{m}}_c(\mathbf{r}) = \hat{\mathbf{q}} \sin \phi + \tilde{\mathbf{m}}_0(\mathbf{r}) \cos \phi. \quad (\text{S5})$$

$\phi$  is the cone angle which is  $\phi = 0$  for the helix and  $\phi \neq 0$  in a conical phase and  $\tilde{\mathbf{m}}_0$  is the helical ansatz from Eq. (S2) in the moving frame. We find that  $\tilde{\mathbf{m}}_c$  indeed is a stationary solution of the moving LLGS equation, Eq.(S4), for

$$\phi = -\text{sign}(\alpha - \beta) \arcsin \left( \frac{\mathbf{v}_e \cdot \hat{\mathbf{q}}}{v_e^{\text{fm}}} \right) \quad (\text{S6})$$

with

$$v_e^{\text{fm}} = \frac{\alpha\gamma(2D - Jq)}{|\alpha - \beta| M_s} > 0 \quad \text{for} \quad 0 < q < 2D/J. \quad (\text{S7})$$

Here,  $v_e^{\text{fm}}$  is the critical drift velocity for which the cone angle closes,  $\phi(v_e^{\text{fm}}) = \pm\pi/2$ , which turns the conical phase into a polarized phase. Note, that this critical drift velocity  $v_e^{\text{fm}}$  depends on  $q$  and is reduced/increased when the helix is squeezed/stretched. In Figure S1, we plot the cone angles  $\phi(v_e)$  up to the critical drift velocities  $v_e^{\text{fm}}$  for different values of  $q$ , including also the instabilities which are discussed in the following section.

This transition from the moving conical state to the polarized state  $\mathbf{m}_p = \pm\hat{\mathbf{q}}$  at  $v_e = v_e^{\text{fm}}$  can be viewed as an analogue of the Walker breakdown of domain walls<sup>S14</sup> for the helical phase. In current-driven domain walls, where two oppositely polarized phases are smoothly connected, the translational mode couples to the helicity mode which is equivalent to the cone angle in the helix. Above a critical current, the helicity of the domain wall is driven far enough out of equilibrium that it cannot be pinned anymore by internal forces which results in a periodic rotation of the magnetization/helicity. In turn, in the ideal helical phase, the Walker breakdown occurs everywhere simultaneously, leading to a polarized state instead of a periodic rotation. In a system with spatial inhomogeneities, however, the Walker breakdown also occurs inhomogeneously which leads to complicated dynamics with strong fluctuations.

Moreover, we can use this result to compute the energy density of the current-driven conical phase as function of  $\mathbf{q}$  and  $\mathbf{v}_e$

$$E(\mathbf{v}_e, \mathbf{q})/\lambda^2 = \frac{\left( \frac{(\alpha - \beta)M_s}{\alpha\gamma} \mathbf{v}_e \cdot \mathbf{q} \right)^2 - q^2(2D - Jq)^2}{2q(2D - Jq)} \quad (\text{S8})$$

which is minimized for

$$q_{\text{opt}}(u_0) = \frac{D}{6J} \left( 10 - \frac{2^{\frac{4}{3}}}{\left( 2 + 27u_0^2 - 3\sqrt{u_0^2(12 + 81u_0^2)} \right)^{\frac{1}{3}}} + 2^{\frac{2}{3}} \left( 2 + 27u_0^2 - 3\sqrt{u_0^2(12 + 81u_0^2)} \right)^{\frac{1}{3}} \right) \quad (\text{S9})$$

where we used  $u_0 = v_e / v_e^{\text{fm}}|_{q=\frac{D}{J}}$  for a shorter notation. However, its meaning remains illusive. A treatment similar to Ref. S15 is not possible in the driven system as stationary solutions are not determined by the minimum of an (effective) energy functional but by the LLGS-induced dynamics.

### Stability of stationary solutions

In the previous section, we found that the moving conical ansatz  $\tilde{\mathbf{m}}_c(\mathbf{r})$ , Eq. (S5), with the current-dependent cone angle  $\phi$ , Eq. (S6), is a stationary solution for the comoving LLGS equation, Eq. (S4), for  $v_e < v_e^{\text{fm}}$ , i.e., it is a fixed point of the system of differential equations. However, it is unclear if this fixed point is *stable* against perturbations or if it is *unstable* such that small perturbations are amplified and drive the system to another fixed point.

The stability is usually analyzed by considering fluctuations around the texture under investigation. Here, we define the ansatz

$$\tilde{\mathbf{m}}_\epsilon(\mathbf{r}, t) = \tilde{\mathbf{m}}_c(\mathbf{r}) + \epsilon (\delta_+(\mathbf{r}, t) \boldsymbol{\psi}_+(\mathbf{r}) + \delta_-(\mathbf{r}, t) \boldsymbol{\psi}_-(\mathbf{r})) , \quad \epsilon > 0 . \quad (\text{S10})$$

where  $\boldsymbol{\psi}_\pm = \frac{1}{\sqrt{2}}(\tilde{\mathbf{m}}_1 \pm i\tilde{\mathbf{m}}_2)$  are gyrating orthogonal perturbations on top of the moving conical solution  $\tilde{\mathbf{m}}_c(\mathbf{r})$ . In our conventions,  $\tilde{\mathbf{m}}_1(\mathbf{r})$  is obtained from  $\tilde{\mathbf{m}}_c(\mathbf{r})$  by  $\phi \rightarrow \phi - \pi/2$ , and  $\tilde{\mathbf{m}}_2(\mathbf{r}) = \tilde{\mathbf{m}}_c(\mathbf{r}) \times \tilde{\mathbf{m}}_1(\mathbf{r})$ . For small perturbations  $\delta \ll 1$ , only terms up to linear order  $\mathcal{O}(\epsilon^1)$  in the moving LLGS, Eq. (S4), are taken into account. The resulting differential equation can be used to determine the excitation spectrum of the current-driven helical/conical phase where the softening of a mode indicates a phase transition.

Most terms in the  $\mathcal{O}(\epsilon^1)$  moving LLGS equation are translation invariant. The broken translational symmetry of the helical phase is only reflected in one term which is proportional to  $\cos(\mathbf{q} \cdot \mathbf{r})$ . Therefore, after casting the equation to Fourier space with the convention

$$\delta(\mathbf{r}, t) = \iint \tilde{\delta}_{\mathbf{k}, \omega} e^{-i\mathbf{k} \cdot \mathbf{r} + i\omega t} d\mathbf{k} d\omega , \quad (\text{S11})$$

with  $\delta(\mathbf{r}, t) = (\delta_+(\mathbf{r}, t), \delta_-(\mathbf{r}, t))$  and  $\tilde{\delta}_{\mathbf{k}, \omega} = (\tilde{\delta}_+(\mathbf{k}, \omega), \tilde{\delta}_-(\mathbf{k}, \omega))$ , the spatial modulation of the helix leads to a coupling between  $\tilde{\delta}_{\mathbf{k}, \omega}$  and the higher modes  $\tilde{\delta}_{\mathbf{k} \pm \mathbf{q}, \omega}$ . Written in terms of  $\mathbf{a}_{\mathbf{k}, \omega} = \tau_1 \tilde{\delta}_{\mathbf{k}, \omega}$ , the  $\mathcal{O}(\epsilon^1)$  moving LLGS equation reads

$$(1 - i\alpha\tau_3)\omega \mathbf{a}_{\mathbf{k}, \omega} = \frac{\gamma}{M_s} \mathcal{M}(\mathbf{k}) \mathbf{a}_{\mathbf{k}, \omega} + \frac{\gamma}{M_s} D k_\perp \sqrt{1 - u_\parallel^2} (\mathbf{a}_{\mathbf{k} + \mathbf{q}, \omega} + \mathbf{a}_{\mathbf{k} - \mathbf{q}, \omega}) \quad (\text{S12})$$

where  $\tau_1$  and  $\tau_3$  are Pauli matrices and the  $2 \times 2$  matrix  $\mathcal{M}(\mathbf{k})$  is given by

$$\mathcal{M}(\mathbf{k}) = \begin{pmatrix} (2D - Jq)(k_\perp u_\perp + \frac{q}{2}(1 - u_\parallel^2)) + J(qk_\parallel u_\parallel + k^2) & \frac{q}{2}(2D - Jq)(1 - u_\parallel^2) \\ -\frac{q}{2}(2D - Jq)(1 - u_\parallel^2) & (2D - Jq)(k_\perp u_\perp - \frac{q}{2}(1 - u_\parallel^2)) + J(qk_\parallel u_\parallel - k^2) \end{pmatrix} . \quad (\text{S13})$$

Here, we write the drift velocity  $\mathbf{v}_e$  in units of the critical drift velocity  $v_e^{\text{fm}}$ , defining  $\mathbf{u} = \text{sign}(\alpha - \beta) \mathbf{v}_e / v_e^{\text{fm}}$ , see Eq. (S6). Moreover, we have written the components of  $\mathbf{k}$  and  $\mathbf{u}$  in terms of their projection onto the conical wave vector  $\hat{\mathbf{q}}$ , such that  $k_\parallel = \mathbf{k} \cdot \hat{\mathbf{q}}$ ,  $k_\perp = \mathbf{k} \cdot (\hat{\mathbf{z}} \times \hat{\mathbf{q}})$ , and similarly  $u_\parallel = \mathbf{u} \cdot \hat{\mathbf{q}}$  and  $u_\perp = \mathbf{u} \cdot (\hat{\mathbf{z}} \times \hat{\mathbf{q}})$ .

We note that the equation for the linear perturbation, Eq. (S12), only has real-valued components except for the prefactor of the frequency  $\omega$  which is complex for a finite Gilbert damping  $\alpha > 0$ . For the analysis of the stability, the imaginary part of the frequency is important, c.f. Eq. (S11): Within our convention, modes with a positive imaginary part of the frequency  $\Im(\omega_\pm) > 0$  are damped and decay exponentially. In turn, modes with  $\Im(\omega_\pm) < 0$  grow exponentially, indicating an instability of the stationary moving conical solution  $\tilde{\mathbf{m}}_c(\mathbf{r})$ .

### Longitudinal instability

Let us first consider an effectively one-dimensional system in which transverse modes  $k_\perp$  are absent and only longitudinal modes  $k_\parallel$  contribute. In this simplified setup, also the coupling between modes vanishes in Eq. (S12). Moreover, because of the simple structure of the mostly real-valued equation, a sign change in the imaginary part of  $\omega$  must occur together with a sign change in the real part. Therefore, obtaining the critical current  $v_{e, \parallel}^{\text{ins}}(k_\parallel)$  in one dimension with the side condition  $\omega = 0$  boils down to solving  $\det(\mathcal{M}) = 0$ . Besides the trivial translational mode,  $k_\parallel = 0$ , we find another solution  $v_{e, \parallel}^{\text{ins}}(k_\parallel)$  which sets the longitudinal instability:

$$\Im(\omega) = 0 \quad \Leftrightarrow \quad k_\parallel = 0 \quad \text{or} \quad v_{e, \parallel}^{\text{ins}}(k_\parallel) = \frac{\alpha\gamma(2D - Jq) \sqrt{q(2D - Jq) + Jk_\parallel^2}}{(\alpha - \beta) M_s \sqrt{2Dq}} \leq v_e^{\text{fm}} . \quad (\text{S14})$$

For currents above the critical drift velocity of the longitudinal instability,  $v_e > v_{e, \parallel}^{\text{ins}}$ , there is a finite range for which  $\Im(\omega(k_\parallel)) < 0$ , i.e., where the helical phase becomes unstable against the condensation of longitudinal modes with  $k_\parallel$  in the interval  $-|k_\parallel^{\text{ins}}| < k_\parallel < |k_\parallel^{\text{ins}}|$ . This instability is indicated in Figure S1 for various values of  $\mathbf{q}$ , assuming an infinitely large system where the mode with  $k_\parallel = 0$  has the lowest critical current.

While the linear stability analysis unveils that the driven helix with a finite cone angle is not a stable fixed point of the LLGS equation for  $v_e > v_{e, \parallel}^{\text{ins}}$ , it is not clear from the analysis to which other stable fixed point, if any, the structure eventually converges. Therefore, we have performed simulations of a one-dimensional system with random noise to check the behavior above the longitudinal instability. The time-resolved realspace dynamics are shown in Figure S1b. It turns out that even for a

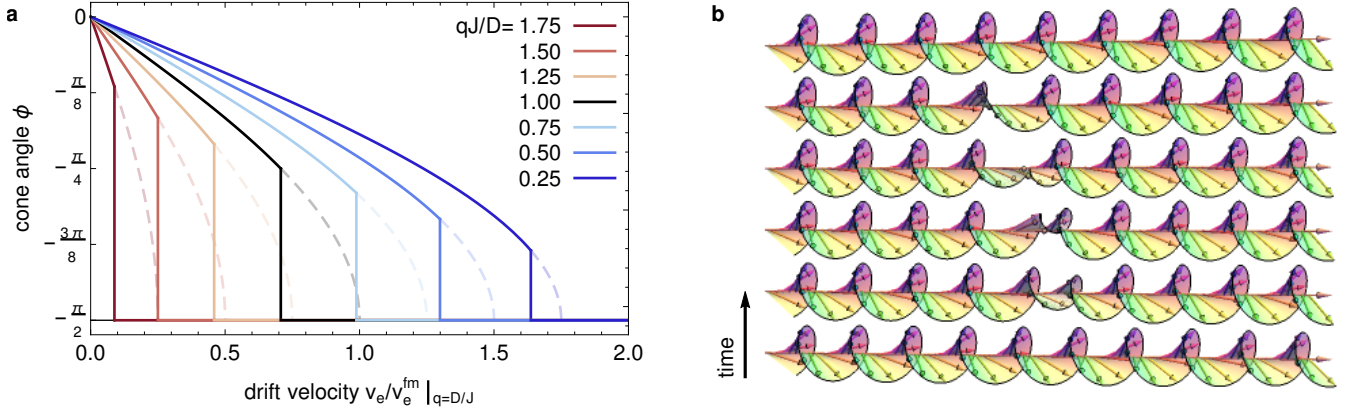


**Fig. S1: Longitudinal instability of the driven helical phase.** **a**, Cone angle  $\phi$  for various values of  $q$ , including the longitudinal instability. Dashed lines indicate  $\phi$  if this instability was absent. **b**, Time-evolution of the driven helical phase above the longitudinal instability as obtained from numerical simulations in one dimension for  $q = D/J$ ,  $|v_e| = 0.72v_e^{\text{fm}}$ ,  $\alpha = 0.1$ , and  $\beta = 0$ . The color encodes the phase, similar to Figure 1 in the main text, but larger cone angles appear more desaturated. The intervals in time are not equidistant and in every panel we shift the texture in the  $x$ -direction to keep the instability approximately centered.

current just slightly above the instability, a longitudinal mode is amplified up to the point where it (smoothly) unwinds one helical soliton. In Figure S1b, this is visible as the reduction from 10 solitons (rotations of the cone) to 9 solitons, which corresponds to change from  $q = D/J$  to  $q = 0.9D/J$ , including an adjustment of the cone angle which is hardly visible by eye. This new state with a reduced  $q < D/J$  has a higher critical current and therefore remains stable.

#### Transverse inherent instability

In two dimensions, in contrast to effectively one-dimensional calculation above, transverse excitations with  $k_{\perp} \neq 0$  in the direction perpendicular to the helical  $q$ -vector couple the different modes and lead to a softer spectrum in this direction<sup>S16</sup>. As we were not able to solve the system of infinitely many coupled modes in Eq. (S12) exactly in two dimensions, we analyzed approximate solutions by following two different routes as explained in the following.

One approach is to truncate the system to only  $n$  neighboring modes with  $\mathbf{k} - n\mathbf{q}, \dots, \mathbf{k}, \dots, \mathbf{k} + n\mathbf{q}$ . The resulting system of linear equations can be represented in a  $(4n + 2) \times (4n + 2)$  matrix which can be diagonalized numerically. Results of this diagonalization for  $n = 10$  are shown in Figure S2a where we plot the imaginary parts of the smallest eigenvalue  $\omega$  as function of  $k_{\perp}$  for  $k_{\parallel} = 0$ . We have checked that  $n = 10$  yields converged results. For small  $u_{\perp}$ , the data collapses onto a universal scaling curve which shows an interval with a  $\Im(\omega) < 0$ , i.e., where the helical phase is unstable.

The second approach is an analytical approximation in the limit of a small perpendicular current  $u_{\perp}$ . We can expand the determinant of the infinitely many coupled equations of Eq. (S12) in powers of  $u_{\perp}$  and find that the relevant physics only happen at order  $\mathcal{O}(u_{\perp}^4)$ , where

$$\Im(\omega) \approx \frac{(-u_{\parallel}^4 + 10u_{\parallel}^2 + 15)k_{\perp}^4 - 8(5 - 2u_{\parallel}^2)u_{\perp}^2k_{\perp}^2 - 16(5 - 2u_{\parallel}^2)u_{\perp}u_{\parallel}k_{\perp}k_{\parallel} + 8(4u_{\parallel}^2(u_{\parallel}^2 - 3) + 5)k_{\parallel}^2}{8\alpha(2u_{\parallel}^4 - 7u_{\parallel}^2 + 5)}. \quad (\text{S15})$$

This function is plotted in Figure S2a as the universal scaling line (red dashed line). From this analytical result in the limit  $u_{\perp} \ll 1$ , we can read off immediately that the sign of the term proportional to  $k_{\perp}^2$  is always negative for reasonable values of  $u_{\parallel} < 1$  which leads to a local minimum at a  $k_{\perp}^{\text{min}} \neq 0$  with  $\Im(\omega(k_{\perp}^{\text{min}})) < 0$ . Therefore, our analytical results confirm the numerical observation that the helical phase is inherently unstable against any finite  $u_{\perp} \neq 0$ . We show the areas of instability in Figure S2b, i.e., the areas in  $\mathbf{k}$ -space where  $\Im(\omega) < 0$ , both for  $u_{\parallel} = 0$  and  $u_{\parallel} > 0$ . Moreover, from Eq. (S15) we can obtain the maximal growth rate of the instability via the minimum of the imaginary part of the spectrum which reads

$$\min(\Im(\omega)) = -\frac{u_{\perp}^4}{\alpha} \frac{2(5 - 7u_{\parallel}^2 + 2u_{\parallel}^4)}{(-1 + 2u_{\parallel}^2)^2(15 + 10u_{\parallel}^2 - u_{\parallel}^4)} \quad \text{at} \quad \begin{pmatrix} k_{\parallel}^{\text{min}} \\ k_{\perp}^{\text{min}} \end{pmatrix} = \frac{2\sqrt{5 - 7u_{\parallel}^2 + 2u_{\parallel}^4}}{\sqrt{15 - 20u_{\parallel}^2 - 21u_{\parallel}^4 + 2u_{\parallel}^6}} \begin{pmatrix} \frac{u_{\parallel}}{2u_{\parallel}^2 - 1}u_{\perp}^2 \\ -u_{\parallel} \end{pmatrix}. \quad (\text{S16})$$

While the instability for  $u_{\perp} \neq 0$  grows exponentially in time, Eq. (S16) reveals that the maximal growth rate of the instability only scales as  $\min(\Im(\omega)) \propto -u_{\perp}^4$  which can result in a very small exponent and, therefore, very long critical time scales at low currents.

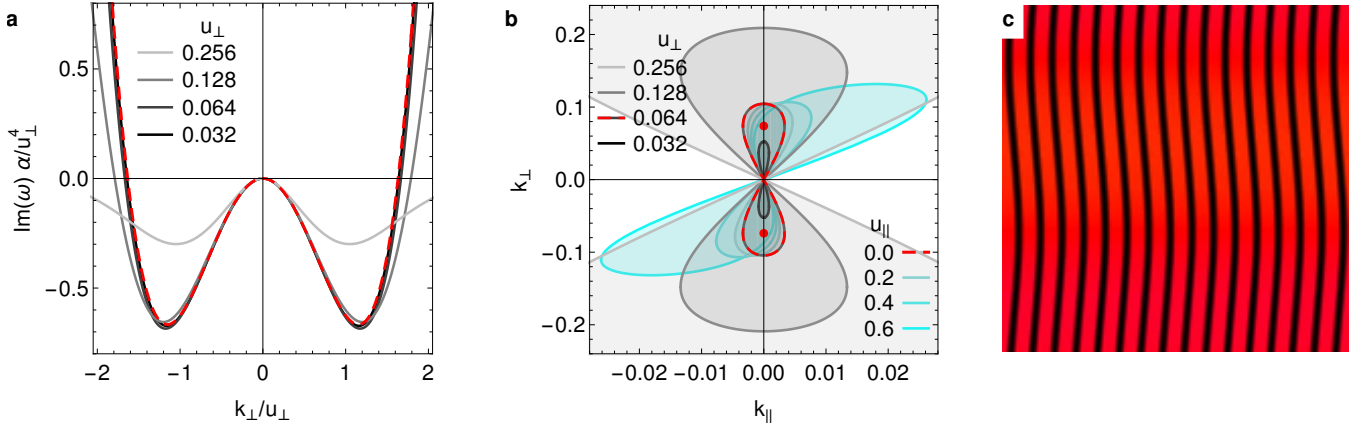


**Fig. S2: Transverse inherent instability of the driven helical phase in more than one dimension.** **a**, Imaginary part of the frequency  $\omega$  as function of the wave vector  $k_{\perp}$  perpendicular to the helical orientation  $\mathbf{q}$  for  $u_{\parallel} = k_{\parallel} = 0$ . Gray lines show the results for  $\alpha = 0.1$  and perpendicular currents  $u_{\perp}$  as indicated, obtained by diagonalizing Eq. (S12) where interactions between modes truncated to  $\mathbf{k} - 10\mathbf{q}, \dots, \mathbf{k}, \dots, \mathbf{k} + 10\mathbf{q}$ . For smaller currents  $u_{\perp} \leq 0.064$  the rescaled curves collapse onto the universal curve (red dashed line) which is analytically calculated in Eq. (S15). **b**, Areas of (in-)stability of the helical phase. Lines indicate solutions of Eq. (S15) for  $\Im(\omega) = 0$ , i.e., where a sign change of the imaginary part of  $\omega$  indicates the transition between a stable regime (outside areas) and an unstable regime (filled areas). Solutions for  $u_{\parallel} = 0$  and various  $u_{\perp} > 0$  are plotted in shades of gray and solutions for  $u_{\perp} = 0.064$  and various  $u_{\parallel} > 0$  are plotted in gray to cyan, as indicated. The data relevant for panel **c** is highlighted by red dashed lines and a red point which indicates the minimum of  $\Im(\omega)$ . **c**, Steady state result of a simulation with  $u_{\parallel} = 0$  and  $u_{\perp} = 0.064$  (c.f., red dashed lines in **b**). Other parameters are  $\alpha = 0.1$  and  $\beta = 0.2$ . The system size is  $16\lambda \times 16\lambda$ . The color code is chosen as in the main text.

The result of a simulation is shown in Figure S2c, following the same color code as in the main text, and was obtained for  $u_{\parallel} = 0$ ,  $u_{\perp} = 0.064$ ,  $\alpha = 0.1$ ,  $\beta = 0.2$ , and a system size of  $16\lambda \times 16\lambda$  with periodic boundary conditions. The wavy helical structure is established as a new steady state, i.e., a new stable fixed point of the LLG equation, after very long simulation times (with these parameters  $\Im(\omega) \approx -10^{-4}$ ). However, in contrast to the one-dimensional scenario, the wavy helical texture remains very closely connected to the equilibrium state.

### Thiele dynamics of defects

In a two-dimensional system, the helix can bend and also host defects, such as disclinations,<sup>S17</sup> dislocations,<sup>S18</sup> or skyrmions.<sup>S19</sup> Whenever the local orientation  $\mathbf{q}$  varies in space, including at such defects, it opens a finite solid angle and thereby creates a finite skyrmion charge density  $w$

$$w = \mathbf{m} \cdot \left( \frac{d\mathbf{m}}{dx} \times \frac{d\mathbf{m}}{dy} \right). \quad (\text{S17})$$

For magnetic skyrmions, the total charge  $Q = (4\pi)^{-1} \int w d\mathbf{r}$  takes integer values,  $Q \in \mathbb{Z}$ , and is known to induce a response velocity which is perpendicular to the driving current or force. The motion of these object, located at position  $\mathbf{R}$  with a quantized topological charge  $Q$ , is well described by the Thiele equation<sup>S20</sup> which reads

$$\mathcal{G} \times (\dot{\mathbf{R}} - \mathbf{v}_e) + \mathcal{D}(\alpha \dot{\mathbf{R}} - \beta \mathbf{v}_e) = \mathbf{F}(\mathbf{R}) \quad (\text{S18})$$

where  $\mathcal{G} = 4\pi Q \hat{\mathbf{z}}$  is the gyrovector and  $\mathcal{D}_{ij} = \int \partial_i \mathbf{m} \cdot \partial_j \mathbf{m} d\mathbf{r}$  is the dissipation matrix.  $\mathbf{F}(\mathbf{R})$  is a force arising from, e.g., the interaction with other magnetic textures. For a recent review we refer to Ref. S21. Solved for the skyrmion velocity, this Thiele equation reads

$$\dot{\mathbf{R}} = \frac{1}{|\mathcal{G}|^2 + \alpha^2 \det(\mathcal{D})} \left( (\alpha - \beta) \mathcal{G} \times \mathcal{D} \mathbf{v}_e + (|\mathcal{G}|^2 + \alpha \beta \det(\mathcal{D})) \mathbf{v}_e - \mathcal{G} \times \mathbf{F}(\mathbf{R}) + \alpha \det(\mathcal{D}) \mathcal{D}^{-1} \mathbf{F}(\mathbf{R}) \right) \quad (\text{S19})$$

where  $\mathcal{D}^{-1}$  is the inverse of the dissipation matrix such that  $\det(\mathcal{D}) \mathcal{D}^{-1}$  is related to  $\mathcal{D}$  via the replacements  $\mathcal{D}_{xx} \rightarrow \mathcal{D}_{yy}$ ,  $\mathcal{D}_{xy} \rightarrow -\mathcal{D}_{xy}$ , and  $\mathcal{D}_{yy} \rightarrow \mathcal{D}_{xx}$ . In the absence of defects or impurities which could break the translational symmetry, i.e., in the limit  $\mathbf{F} = 0$ , we can also use this Thiele equation to determine the velocity of the charge-free helical phase which simply evaluates to

$$\dot{\mathbf{R}} = \frac{\beta}{\alpha} \mathbf{v}_e \quad \text{for } Q = 0 \text{ and } \mathbf{F} = 0. \quad (\text{S20})$$

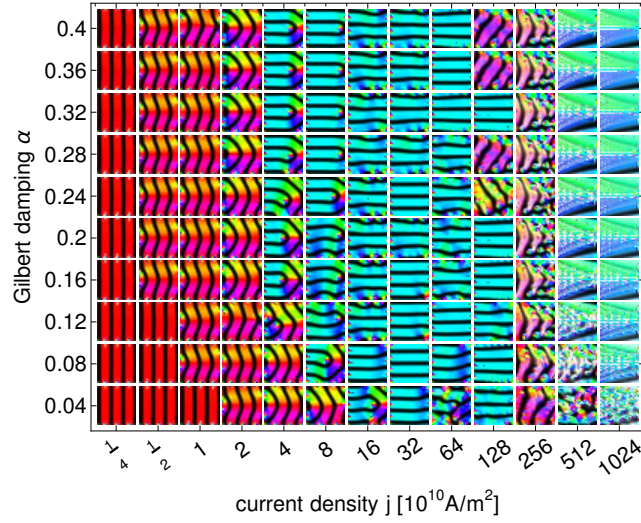


**Fig. S3: Current-induced steady-state magnetization in an MRAM cell.** Panels show the magnetization in a  $3\frac{1}{4}\lambda \times 3\frac{1}{4}\lambda$  MRAM cell during a current pulse. The original state "0" is shown in the main text and the current  $v_e$  is applied to the right. The setup is the same as in the main text, Figure 6b, which shows the magnetization after switching off the current.

In contrast to the standard setup of skyrmions in a polarized background, however, topological charges in the helical phase are not embedded in a translation invariant background. Instead, the surrounding helical modulation breaks this symmetry and translations of defects are not (approximately) zero modes of the system. Moreover, the topological charges of dislocations, as shown in Figures 3b and c in the main text, are not quantized and it is questionable whether these objects can be viewed as localized defects.

Nevertheless, we can still consult the Thiele equation to gain at least qualitative insight into the motion of defects. As depicted in Figures 3d-f in the main text, topological charges are quite well localized on dislocations and skyrmions which can accumulate at phase boundaries or appear as single defects inside a helical phase. In the absence of forces,  $\mathbf{F} = 0$ , the first term of Eq. (S19) induced a charge-dependent perpendicular velocity, similar to the skyrmion Hall effect for skyrmions. For the setup used throughout this paper where  $\mathbf{v}_e = v_e \hat{x}$ , this translates to

$$\text{sign}(\dot{Y}) = \text{sign}(\alpha - \beta) \text{sign}(Q) \text{sign}(v_e) \quad \text{for } \mathbf{v}_e = v_e \hat{x}, \quad (\text{S21})$$

which is also shown in Figures 3e-f as white arrows. This qualitative result is in agreement with the observed motion in the simulations, see Supplementary Movie S2. Moreover, for  $\alpha \neq \beta$ , the defects have a different *parallel* velocity than the surrounding helical phase which is compensated by a force  $\mathbf{F}(\dot{\mathbf{R}}_d - \dot{\mathbf{R}}_h)$  where  $\dot{\mathbf{R}}_d$  is the velocity of the defect and  $\dot{\mathbf{R}}_h$  is the velocity of the surrounding helix which may be given by Eq. (S20) in a setup with a low density of defects. This extra force leads to an additional charge-dependent perpendicular drift of the defects, which leads to a similar contribution as in Eq. (S21). As for sufficiently small currents a dislocation is tied to a helical soliton, this charge-driven transverse motion leads to a *combing* of the helical phase into the observed perpendicular pattern.

### The helical orientation based MRAM element

In the main text, we have proposed an MRAM-like magnetic cell which can encode information based on the orientation of the helical phase. However, the phase diagram in Figure 6b in the main text only shows data after a long current pulse for a  $3\frac{1}{4}\lambda \times 3\frac{1}{4}\lambda$  square-shaped cell with a damping ratio  $\beta/\alpha = 2$ , which leads to both strong defect dynamics and a high velocity of the helical phase. The steady states which establish during this long current pulse are shown in Figure S3.

Here, we also present more phase diagrams of this type for other settings, namely a different ratio  $\beta/\alpha = 1$  (instead of  $\beta/\alpha = 2$ ) in Figure S4 and a larger cell size of  $6\frac{1}{4}\lambda \times 6\frac{1}{4}\lambda$  (instead of  $3\frac{1}{4}\lambda \times 3\frac{1}{4}\lambda$  in Figure S5). When comparing the data, it is necessary to notice that the data in the main text is shown as function of the current density  $\mathbf{j}$  whereas it is a function of the drift velocity  $\mathbf{v}_e$  which includes a conversion factor  $1 + \beta^2$  which changes in every row of the diagram because we fixed the ratio to  $\beta/\alpha$ .

In Figure S4 we focus again on the rather small  $3\frac{1}{4}\lambda \times 3\frac{1}{4}\lambda$  element but with  $\beta = \alpha$ , i.e., with suppressed defect dynamics. In fact,  $\beta = \alpha$  renders the LLGS equation Galilei invariant, which means that without edges the entire magnetization would move at a velocity  $\mathbf{v} = \mathbf{v}_e$  but remain static in the comoving frame of reference. Here, in a small cell, the translational invariance

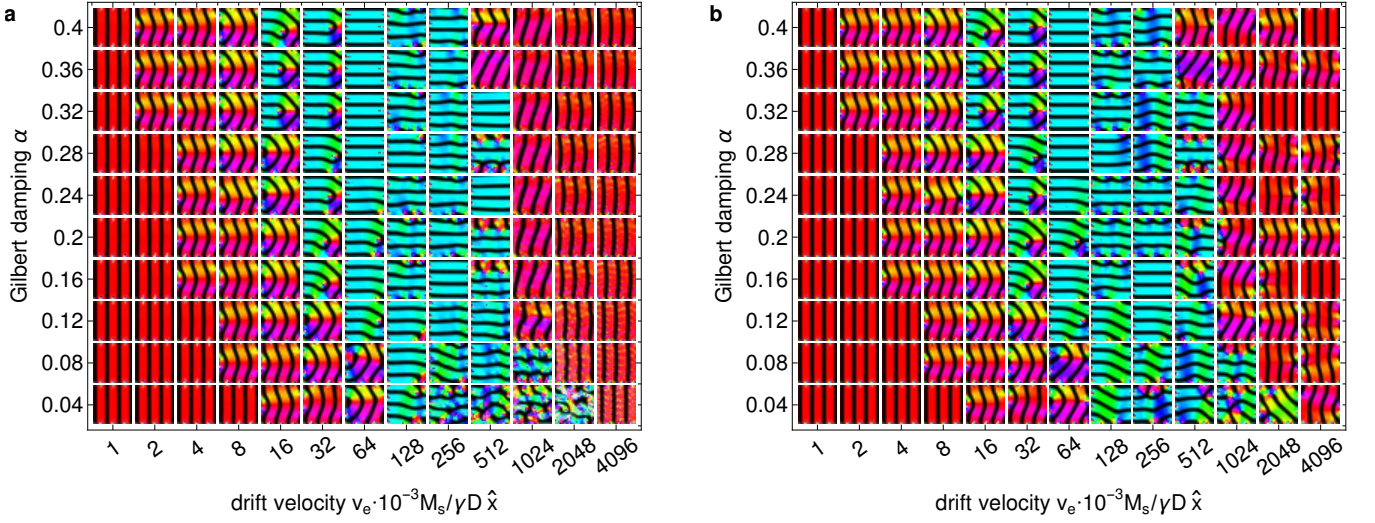


**Fig. S4: A magnetic memory based on the helical orientation:  $\alpha = \beta$ .** Panel **a** shows the steady-state magnetization which establishes while a current is applied and **b** shows the magnetization long after the current pulse. The plot indicates the switching success for various current strengths  $v_e$  and Gilbert dampings  $\alpha$  for  $\beta = \alpha$  on a  $3\frac{1}{4}\lambda \times 3\frac{1}{4}\lambda$  element. The original state "0" is shown in the main text and the current  $v_e$  is applied to the right. The results for very high current densities should be taken with caution as the numerics showed strong fluctuations even for very small time-discretizations.

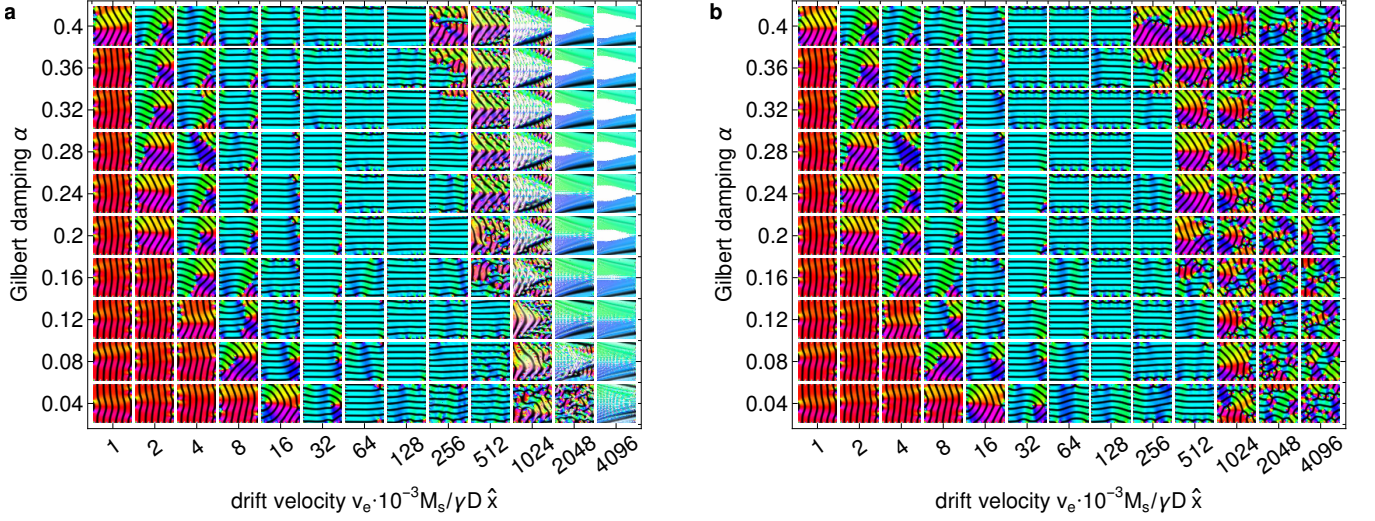


**Fig. S5: A magnetic memory based on the helical orientation: larger cell size.** Panel **a** shows the steady-state magnetization which establishes while a current is applied and **b** shows the magnetization long after the current pulse. The plot indicates the switching success for various current strengths  $v_e$  and Gilbert dampings  $\alpha$  for  $\beta = 2\alpha$  on a  $6\frac{1}{4}\lambda \times 6\frac{1}{4}\lambda$  element. The original state "0" is shown in the main text and the current  $v_e$  is applied to the right.

is broken by the edges which can still induce order. For small currents, we find that the critical current for switching is indeed approximately a factor 2 higher compared to the data with  $\beta/\alpha = 2$  from the main text, which is in accordance with the now smaller helical drift velocity in the absence of defects. For high currents, we do not observe the approximate inplane polarization of the element. However, this data for high currents should be treated cautiously as the numerics were subject to large changes of the magnetization even for very small time-stepping which is indicative of a large numerical error.

In Figure S5 we consider a larger  $6\frac{1}{4}\lambda \times 6\frac{1}{4}\lambda$  element with the ratio  $\beta/\alpha = 2$  from the main text. The larger system can host a larger number of helical solitons (appearing as black stripes in the panels). This also leads to an enhanced set of critical currents for pushing the initial texture out of the system, which is not resolved on the sparse dataset shown here. In particular, the plot confirms that the lowest critical currents for partially expelling the initial phase decrease significantly when the system

size increases.

- 
- <sup>S1</sup> Beg, M. et al. Ground state search, hysteretic behaviour and reversal mechanism of skyrmionic textures in confined helimagnetic nanostructures. *Sci. Rep.* **5**, 17137 (2015).
- <sup>S2</sup> Dzyaloshinskii, I. E. The Theory of Helicoidal Structures in Antiferromagnets. II. Metals. *J. Exp. Theor. Phys.* **20**, 223 (1965).
- <sup>S3</sup> Fert, A. & Levy, M. Role of Anisotropic Exchange Interactions in Determining the Properties of Spin-Glasses. *Phys. Rev. Lett.* **44**, 1538 (1980).
- <sup>S4</sup> Crépieux, A. & Lacroix, C. Dzyaloshinsky-Moriya interactions induced by symmetry breaking at a surface. *J. Magn. Magn. Mater.* **182**, 341–349 (1998).
- <sup>S5</sup> Wessely, O., Skubic, B. & Nordström, L. Spin-transfer torque in helical spin-density waves. *Phys. Rev. B* **79**, 104433 (2009).
- <sup>S6</sup> Proskurin, I. V., Ovchinnikov, A. S. & Kishine, J. Field-Like spin-transfer torque in a chiral helimagnet. *J. Exp. Theor. Phys.* **111**, 236–240 (2010).
- <sup>S7</sup> Slonczewski, J.C. Current-driven excitation of magnetic multilayers. *J. Magn. Magn. Mater.* **159**, L1–L7 (1996).
- <sup>S8</sup> Berger, L. Emission of spin waves by a magnetic multilayer traversed by a current. *Phys. Rev. B* **54**, 9353 (1996).
- <sup>S9</sup> Gilbert, T. A phenomenological theory of damping in ferromagnetic materials. *IEEE Trans. Magn.* **40**, 3443–3449 (2004).
- <sup>S10</sup> Zhang, S. & Li, Z. Roles of Nonequilibrium Conduction Electrons on the Magnetization Dynamics of Ferromagnets. *Phys. Rev. Lett.* **93**, 127204 (2004).
- <sup>S11</sup> Bazaliy, Y. B., Jones, B. A. & Zhang, S.-C. Modification of the Landau-Lifshitz equation in the presence of a spin-polarized current in colossal- and giant-magnetoresistive materials. *Phys. Rev. B* **57**, R3213(R) (1998).
- <sup>S12</sup> Barnes, S. E. & Maekawa, S. Current-Spin Coupling for Ferromagnetic Domain Walls in Fine Wires. *Phys. Rev. Lett.* **95**, 107204 (2005).
- <sup>S13</sup> Masell, J., Rodrigues, D. R., McKeever, B. F. & Everschor-Sitte, K. Spin-transfer torque driven motion, deformation, and instabilities of magnetic skyrmions at high currents. *Phys. Rev. B* **101**, 214428 (2020).
- <sup>S14</sup> Schryer, N. L. & Walker, L. R. The motion of 180° domain walls in uniform dc magnetic fields. *J. Appl. Phys.* **45**, 5406 (1974).
- <sup>S15</sup> Bauer, A. et al. Symmetry breaking, slow relaxation dynamics, and topological defects at the field-induced helix reorientation in MnSi. *Phys. Rev. B* **95**, 024429 (2017).
- <sup>S16</sup> Belitz, D., Kirkpatrick, T. R. & Rosch, A. Theory of helimagnons in itinerant quantum systems. *Phys. Rev. B* **73**, 054431 (2006).
- <sup>S17</sup> Schoenherr, P. et al. Topological domain walls in helimagnets. *Nat. Phys.* **14**, 465–468 (2018).
- <sup>S18</sup> Dussaux, A. et al. Local dynamics of topological magnetic defects in the itinerant helimagnet FeGe. *Nat. Commun.* **7**, 12430 (2016).
- <sup>S19</sup> Müller, J. et al. Magnetic Skyrmions and Skyrmion Clusters in the Helical Phase of Cu<sub>2</sub>OSeO<sub>3</sub>. *Phys. Rev. Lett.* **119**, 137201 (2017).
- <sup>S20</sup> Thiele, A. A. Steady-State Motion of Magnetic Domains. *Phys. Rev. Lett.* **30**, 230 (1973).
- <sup>S21</sup> Masell, J. & Everschor-Sitte, K. Current-Induced Dynamics of Chiral Magnetic Structures: Creation, Motion, and Applications. Preprint at <https://arxiv.org/abs/2004.13535> (2020)